Physics of the Earth and Planetary Interiors 346 (2024) 107125

Contents lists available at ScienceDirect

Physics of the Earth and Planetary Interiors

journal homepage: www.elsevier.com/locate/pepi

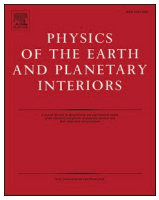

Dislocations in naturally deformed olivine: Example of a mylonitic peridotite

Sylvie Demouchy [a,b,*], Alexandre Mussi [c], Timmo Weidner [c], Emmanuel Gardés [b], Patrick Cordier [c,d]

[a] Géosciences Montpellier, Université de Montpellier & CNRS, UMR 5243, Montpellier F-34095, France
[b] Laboratoire Magmas et Volcans, Université Clermont Auvergne, CNRS, IRD & OPGC, UMR 6524, Aubière F-63170, France
[c] Univ. Lille, CNRS, INRAE, Centrale Lille, UMR 8207 - UMET - Unité Matériaux et Transformations, Lille F-59000, France
[d] Institut Universitaire de France, Paris F-75005, France

ARTICLE INFO

Keywords:
Olivine
Peridotite
Mylonite
Oman
Dislocation
TEM
Tomography
Melt
Bubble

ABSTRACT

We have investigated the microstructure of naturally deformed olivine (chemically equilibrated at 1000 °C) by conventional transmission electron microscopy and electron tomography. The peridotite specimen, from Oman ophiolite, has a mylonitic microstructure with remnant, strongly deformed, millimetric porphyroclasts co-existing with small newly formed olivine grains generated by dynamic recrystallization. Imaging by transmission electron microscopy reveals that both newly formed grains and porphyroclasts display [100] and [001] dislocations activity. Subgrain boundaries are composed of either [100] or [001] dislocations. The characterization of this natural sample also permits to identify sporadic [100] dislocation loops, rare [010] dislocation, infrequent melt, and intragranular bubbles or along subgrain boundaries. Electron tomography permits to identify several glide planes, which are similar to previous observations acquired on experimentally deformed polycrystalline olivine, more importantly electron tomography also permits to evidence combination of glide, climb and mixed climb (dislocation moving in an intermediate plane between the plane of glide plane and the plane of pure climb). Our study further infers the diversity of linear defects responsible for plastic deformation of olivine at lithospheric conditions.

1. Introduction

Rheological properties of olivine control the relative rigidity of the lithospheric plates, which are mostly composed of olivine-rich rocks (90%), but also the lower viscosity of the asthenosphere beneath the lithospheric plates. Consequently, the fundamental mechanisms of the elastic, plastic and brittle deformation of olivine have been the subject of many investigations over the past half-century. Many different approaches were employed, from the study of natural mantle-derived olivines (e.g., Carter and Ave'Lallemant, 1970; Green, 1976; Gueguen, 1977; Ben Ismail and Mainprice, 1998), to deformation experiments performed in the laboratory (e.g., Raleigh, 1968; Gaboriaud et al., 1981; Bai and Kohlstedt, 1992; Couvy et al., 2004; Idrissi et al., 2016; Thieme et al., 2018: Demouchy et al., 2023) or using numerical modeling (e.g., Durinck et al., 2007; Boioli et al., 2015a, 2015b; Gouriet et al., 2019; Mahendran et al., 2017, 2019). Due to the nanoscale nature of the defects involved in permanent deformation of minerals, characterization at micro- to nano-scale has been challenging, although it represents an invaluable source of information. Here, this study focuses on natural occurrence of dislocations in mantle-derived, naturally deformed peridotite. We assume that the microstructure is still representative of the conditions at depth, without significant modification below 1000 °C. The motion of dislocation, by glide and/or climb is considered to control the large-scale creep flow in mantle minerals such as olivine with millimetric grain size (e.g., Poirier, 1985, p.136–138, p.189–190). The characterization of these linear defects (Burgers vector [uvw] and plane (hkl) of glide and/or climb) has been investigated by transmission electron microscopy (TEM) for decades in metals, and the same techniques were employed for minerals such as silicates (Wenk, 1976; McLaren, 1991; Cordier, 2013). Furthermore, decoration at high temperature coupled to optical microscopy (Kohlstedt et al., 1976) or imaged using scanning electron microscopy (Karato, 1987) was also

* Corresponding author at : Laboratoire Magmas et Volcans, Université Clermont Auvergne, Campus Universitaire des Cézeaux, 6 Avenue Blaise Pascal, TSA 60026 - CS 60026, 63178 AUBIERE Cedex, France.
E-mail address: sylvie.demouchy@uca.fr (S. Demouchy).

https://doi.org/10.1016/j.pepi.2023.107125
Received 23 May 2023; Received in revised form 2 December 2023; Accepted 3 December 2023
Available online 7 December 2023

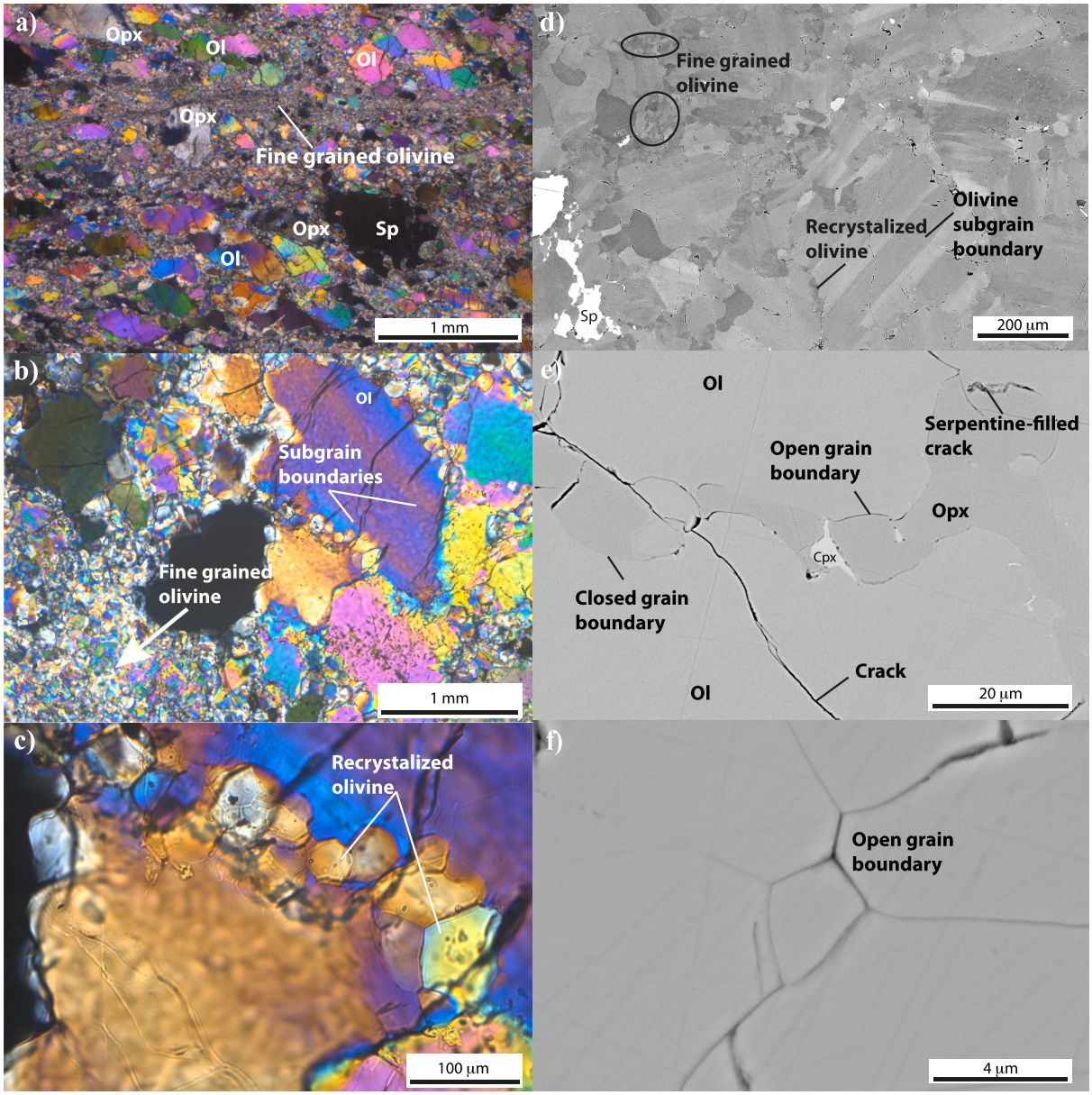

Fig. 1. Optical microphotographs of the studied peridotite from Oman, showing (a) fine-grained olivine (Ol) matrix, olivine porphyroclasts with subgrain boundaries formed by plastic deformation, orthopyroxene (Opx) and spinel (Sp); (b) and (c) details showing the fine-recrystallized olivine at the border of a porphyroclast; (d) electron backscatter image showing large porphyroclasts with internal array of subgrain boundaries and areas with recrystallized olivine as well as cracks and rare pluck out grains; (e) and (f) electron backscatter image showing close and open grain boundaries, cracks cross-cutting grains, and filled with secondary serpentine.

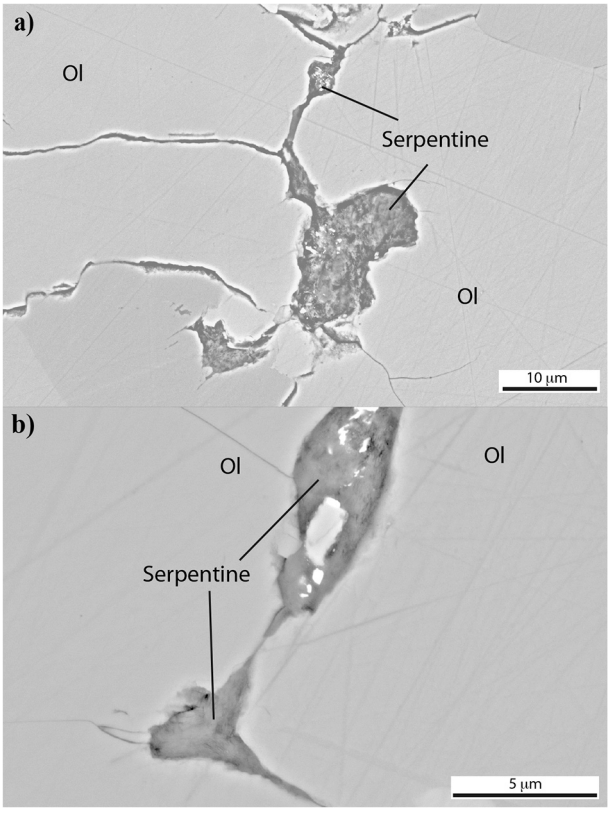

Fig. 2. (a) and (b) Electron backscatter image showing intergranular cracks and olivine (Ol) grain boundaries filled up with serpentine mixture (identified using Fourier transformed spectrometry, and TEM, see main text for details).

used successfully. Recently, electron channelling contrast imaging (Miyajima et al., 2018) has provided successful outcomes for characterizing dislocations. We recall that the current knowledge on identification of dislocations was mostly established on experimentally deformed single crystal. Moreover, the aim of these laboratory deformation experiments was to establish the impact of specific intrinsic or extrinsic parameters such as temperature (e.g., Raleigh, 1968; Demouchy et al., 2013), pressure (e.g., Couvy et al., 2004), silica activity or oxygen fugacity (e.g., Bai et al., 1991), water activity (e.g., Mackwell et al., 1985; Jung and Karato, 2001) and even co-existence with melt (e.g., Kohlstedt et al., 2000; Holtzman et al., 2003). We briefly recall the main features of dislocations in olivine below (see for review Green, 1976; Gueguen and Nicolas, 1980; Demouchy, 2021). In olivine, dislocation slip directions were theoretically established based on the orthorhombic crystallographic lattice (a = 4.76 Å, b = 10.22 Å, c = 5.66 Å) leading to two most favorable Burgers vectors [100] and [001] (the shortest lattice repeats) over a significantly less favorable [010] Burgers vector. While observation of [100] and [001] dislocations is common (e.g., Carter and Ave'Lallemant, 1970; Mussi et al., 2014, 2015, 2017), observation of [010] dislocations remains extremely infrequent (Goetze and Kohlstedt, 1973; Fujino et al., 1993). Recent investigations by electron tomography have further allowed for an assessment of the diverse glide planes for both [100] and [001] dislocations (e.g., Demouchy et al., 2014; Mussi et al., 2014, 2015, 2017): [100](010); [100](001); [100](041); [100](021); [100](011); [001](100); [001](010); [001]{110}; [001](140); [001](130); and [001](120). The relative activity of these different slip systems is of course a function of the applied stress, but also of temperature. Below 1000 °C, [001] dislocations glide in the {110} and (100) planes (Raleigh, 1968). At 1000 °C, activation of [100] dislocation occurs, but the dominant glide planes change to $\{0kl\}$. The [001] glide starts to be active again for high differential stresses (>100 MPa, e.g., Demouchy et al., 2014). At high temperatures, such as those typical of the Earth's asthenosphere (>1200 °C, and low differential stress, 1–10 MPa), the dominant slip systems in olivine involve [100] glide (Raleigh, 1968; Gueguen, 1979; Couvy et al., 2004; Demouchy et al., 2013). At even higher temperature (>1300 °C), the diffusion coefficient of Si, which is controlled by the product of Si vacancy concentration and vacancy diffusivity (Nakamura and Schmalzried, 1983; Poirier, 1985, p. 42, see his eq. 2.13, J. Philibert, 1991) and by extension jog mobility (Poirier, 1985, p. 58), is significantly enhanced up to the point where jogs are not negligible anymore. Thus, at these high temperatures the dislocation climb mechanism unlocks edge [100] dislocations in olivine (e.g., Goetze and Kohlstedt, 1973). Furthermore, numerical modeling of dislocation dynamics in 2.5 dimensions has shown that only a small amount of climb is actually required (<0.1% of the strain) to maintain an efficient, steady-state like, dislocation glide at macroscale in olivine single crystals (e.g., Boioli et al., 2015a, 2015b; Gouriet et al., 2019). We remind that with increasing stress and strain, the accumulation of intragranular dislocations triggers recovery processes, such as the formation of subgrain boundaries (also called dislocation walls), a feature commonly observed in naturally deformed olivine-rich rocks.

The study of naturally deformed olivine has been the subject of pioneering investigations in the seventies (e.g., Carter and Ave'Lallemant, 1970; Green, 1976; Gueguen, 1977, 1979; Gueguen and Darot, 1980). They established the activity of both [100] and [001] dislocations in peridotite xenoliths from various settings (transported by alkali basalt, kimberlite or massif peridotites), most of them being representative of a low-temperature regimes typical of the uppermost mantle (900–1150 °C). Taking into consideration uncertainties on equilibrium temperatures (± 1000 °C for spinel-bearing peridotites, Brey and Köhler, 1990), these observations agree with results from experimentally deformed olivine crystals. Here, we further characterize a naturally deformed peridotite, from an ultra-fresh massif peridotite exhumed tectonically into crustal conditions by conventional transmission electron microscopy (CTEM). Moreover, we use electron tomography to further assess dislocation activity in a natural environment, where multiple intrinsic or extrinsic parameters co-exist and compete.

2. Material and methods

2.1. Peridotitic mylonites from Oman

The mantle peridotite specimen investigated here (sample 98OA87) is a naturally deformed spinel-bearing harzburgite collected from a mylonitic zone in the Wuqba massif in the Oman ophiolite (Nicolas and Boudier, 1995). This mylonitic zone has a km-scale and is a typical low-temperature shear zone chemically equilibrated at ~1000 °C (based on element partitioning, e.g., Brey and Köhler, 1990). Since ionic mobility and dislocation recovery are both very limited below this temperature, we assume that the microstructure was also equilibrated at ~1000 °C (e.g., Costa and Chakraborty, 2008; Farla et al., 2011) and not significantly modified during post-tectonic emplacement. This specific mylonite was already used as an experimental starting material for deformation experiments in traction (Ben Ismail et al., 2021). Our choice was motivated by the characterization of a natural peridotite with distinct deformation features and not being completely dislocation-free due to static annealing at high temperature (≥ 1200 °C). The peridotite has a weak texture and a relatively homogeneous olivine-rich mineralogical assemblage, with 75% olivine (Ol, Mg# = 91; Mg# = 100 × (Mg + Fe)/Mg); 20% orthopyroxenes (Opx); 3% clinopyroxenes (Cpx) and 2% Cr-rich spinel (Sp); locally it can contain up to 90% olivine. The spinel-bearing harzburgite is a fine-grained mylonite with a well-developed lineation and foliation marked by shape preferred orientation of olivine porphyroclasts and sometime enstatite porphyroclasts as illustrated by Fig. 1. The multi-millimetric porphyroclasts display undulose extinction, numerous sub-grain boundaries and irregularly shaped grain

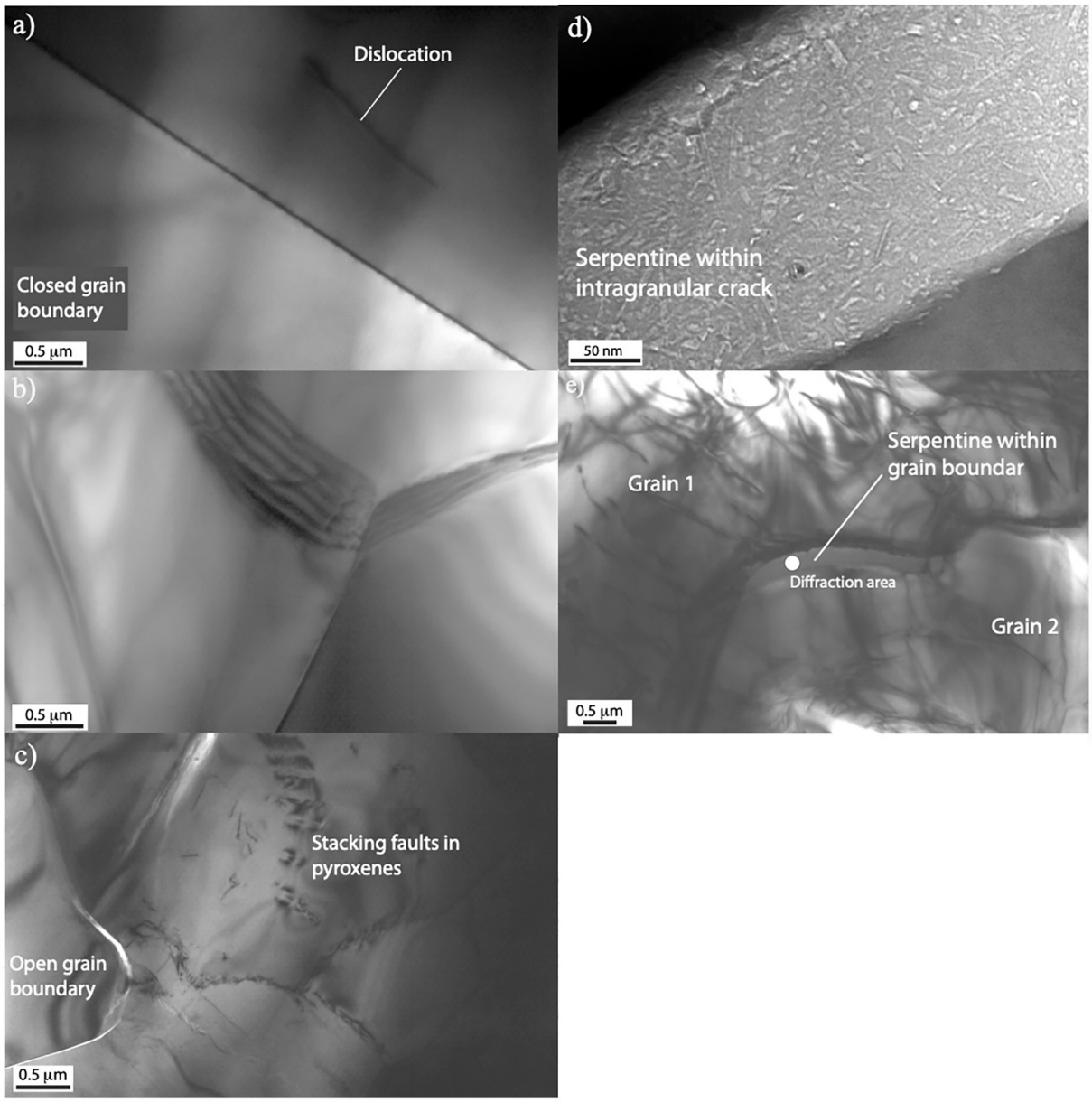

Fig. 3. Representative TEM images of typical grain boundaries. (a) Bright field image of a clean grain boundary adjacent to two olivine grains, with very low dislocation density; (b) bright field image of a clean and closed triple junctions of olivine, again with very low dislocation density; (c) bright field image of an example of open grain boundary between olivine and orthopyroxene, with the latter contain stacking faults; (d) bright field image of serpentine along a crack cross cutting an olivine grain; (e) bright field image of a zone used for selection area electron diffraction (SAED) to identified serpentine between two dislocation-bearing grains.

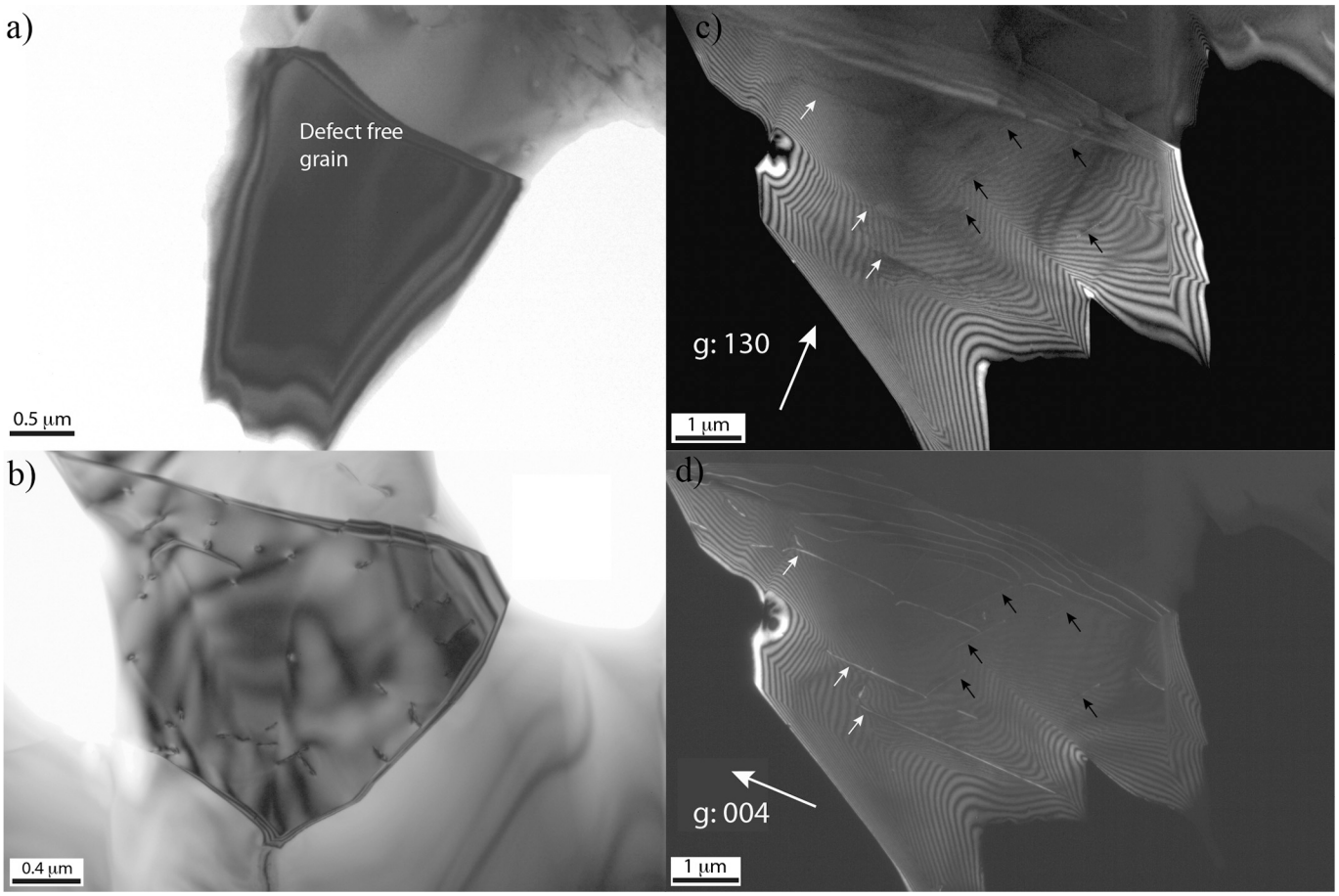

Fig. 4. TEM images of typical microstructure of newly formed olivine grains with dislocation-free grain and grains with dislocation density from 10^{10} m^{-2} up to 10^{12} m^{-2} (for these fields of view). (a) Bright field image of a dislocation-free newly formed grain; (b) weak-beam dark field image showing low dislocation activity; (c) another newly formed olivine grain imaged in weak-beam dark field showing [100] dislocation activity (black arrows); (d) weak-beam dark field image of the same grain as in (c) showing [001] dislocation activity (white arrows).

boundaries (Fig. 1a-d), while the matrix is mainly composed of small newly formed olivine grains (1–20 µm, Fig. 1c) with equilibrated triple junctions (Fig. 1c and f). The pyroxenes have cuspate shape, typical of past percolating melt (Fig. 1e) (e.g., Hidas et al., 2016).

We briefly detail below the main petrographic features of this mylonite previously reported in Ben Ismail et al. (2021): olivine displays a weak crystallographic preferred orientation (CPO) characterized by weak alignment of [100] parallel to the lineation marked by the elongation of the porphyroclasts. The composition and microstructure of this mylonite indicate a depleted oceanic lithosphere source, deformed at temperature < 1000 °C, in a shear zone normal to the ridge axis (see Nicolas and Boudier, 1995). While optical microscopy investigation did not reveal significant alteration, previous analyses by unpolarized Fourier transformed infrared spectroscopy (FTIR) revealed minor serpentinization along grain boundaries and fractures, with OH band at 3690 cm^{-1}, typical of lizardite (Post and Borer, 2000), although no pervasive presence of melt is noted at this scale (see Ben Ismail et al., 2021 for infrared spectroscopy method and representative unpolarized spectra).

2.2. Sample preparations

A couple of thin sections were prepared for optical microscopy and TEM (thickness < 30 µm, polished on both sides and glued with Crystalbond™) and one thick doubled polished section was prepared for both FTIR (500 µm thick prepared with crystal bound) and scanning electron microscopy (SEM). In all cases, the polishing stages include a final chemo-mechanical polish with colloidal silica (0.04 µm particles, average polishing duration of 1 h).

2.3. Scanning electron microscopy

Following FTIR analysis, the thick polished section is prepared for SEM investigation by deposition of a $\sim$ 20 nm carbon layer. The section is then mounted on a SEM stub using carbon double tape. Backscattered electron images were acquired at 10 kV and 0.8 nA using the focused ion beam-scanning electron microscope ThermoFisher® Helios 5 PFIB CXe at the University Clermont Auvergne (France).

2.4. Transmission electron microscopy

During this investigation, we have used different acquisition methods in conventional transmission electron microscopy (CTEM): bright field, weak-beam dark field (WBDF), scanning TEM (STEM). Furthermore, WBDF was associated with precession for electron tomography (e.g., Mussi et al., 2014, 2015, 2017). We recall briefly below the imaging conditions.

2.4.1. Conventional transmission electron microscopy

CTEM was primarily used to characterize the microstructures of the naturally deformed peridotite. Several copper grids were glued on the surface of the thin sections using araldite. Afterwards, the crystal bound

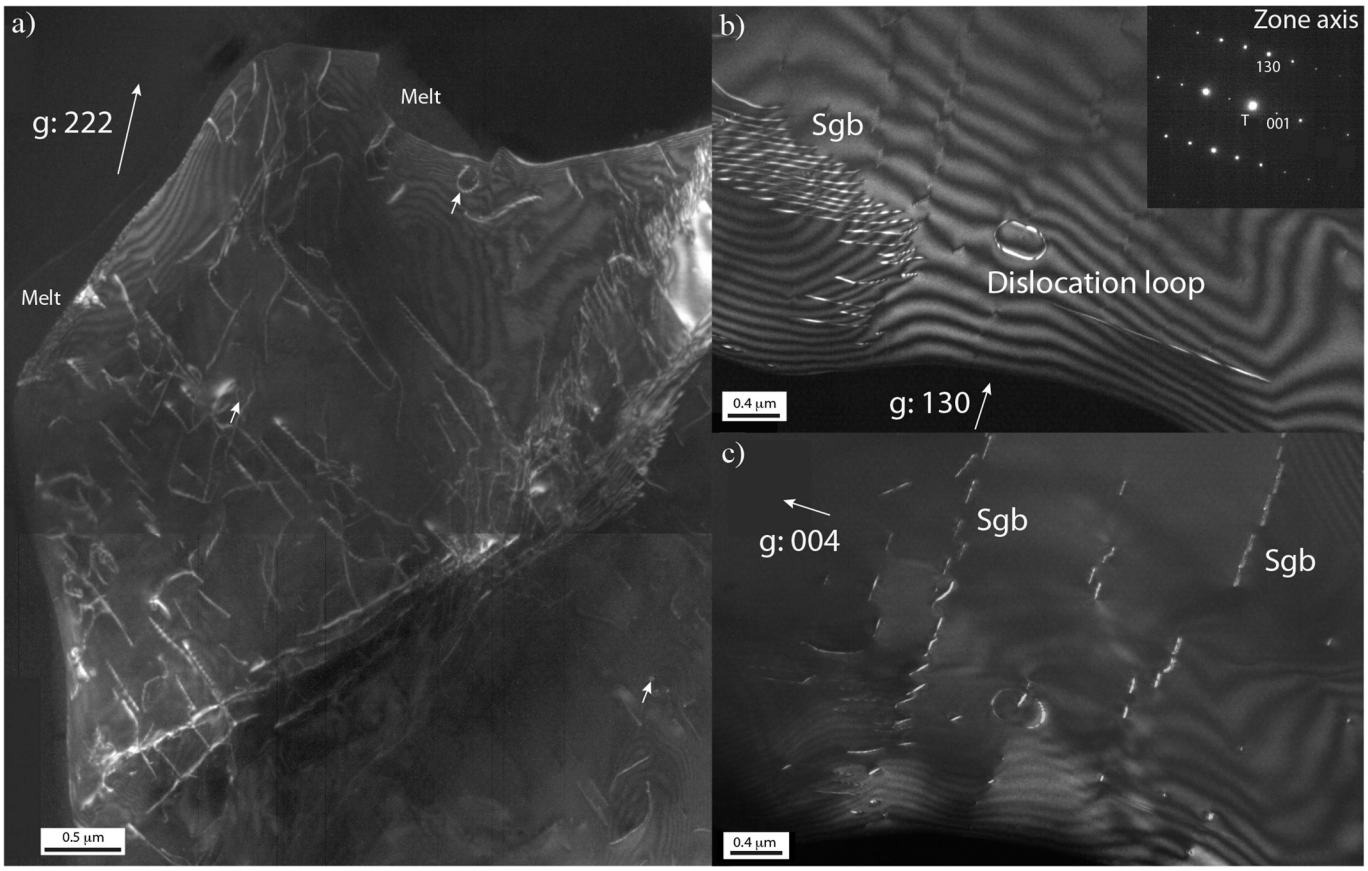

Fig. 5. (a) Weak-beam dark field TEM images of olivine porphyroclasts (dislocation density $\approx 3 \times 10^{13}$ m^{-2}) showing typical microstructure with both [100] and [001] dislocation images using g:222; (b) and (c) showing typical picket-fence feature of subgrain boundary (Sbg) wall composed of either [100] and [001] dislocation, respectively. Rare [100] dislocation loops are also found (central top of (a) and in (b) and (c)). The short white arrows are pointing at dislocation loops.

was dissolved in acetone. Subsequently, the selected samples mounted on Cu grids were Ar-ion milled at 5 kV under a low beam angle of 7° using a Gatan® precision ion polishing system. Several holes formed with adequate electron transparency at their borders. The foils were subsequently covered with a thin layer of carbon to ensure electron conductivity. TEM observations were carried out at the University of Lille (France) using a FEI® Tecnai G^{2}20 TWIN microscope operating at 200 kV.

2.4.2. *Electron tomography of dislocations*

Dislocation electron tomography (DET) is a powerful technique for reconstructing the 3D microstructure of dislocations (Barnard et al., 2006). Unlike conventional tomographic studies, DET is based on diffraction contrast, which necessitates a high orientation precision. To get well-contrasted dislocations, a diffraction vector with a high structure factor must be selected. In this study, we have selected the $13\bar{1}$ diffraction vector, the third more intense structure factor in the olivine structure which allows to visualize both [100] and [001] dislocations. To perform DET, a tilt-series is acquired along this diffraction vector which must be perfectly aligned with the tilt axis to maintain constant diffraction contrast conditions throughout the acquisition of image series. An accuracy of $\pm 0.1°$ is necessary for a successful alignment. The micrographs were taken in WBDF to achieve a high signal-to-noise ratio, and with a precession angle of 0.15° to enhance dislocation contrast as this homogenizes the background by removing most of the thickness fringes and to reduce the oscillating contrast of inclined dislocations (Rebled et al., 2011). The method was fully presented in Mussi et al. (2014, 2015). The tilt-series was acquired every 2° from −40° to 50° in a double-tilt sample holder. Note that the contrasts of WBDF micrographs are in general too weak to allow automatic alignments, post-acquisition image treatment is required to improve the dislocation contrast and obtain a valuable reconstructed volume. Dislocation contrast is enhanced using the "rolling ball" tool, accessible in the ImageJ software (Schindelin et al., 2012). We used the weighted back projection (WBP) algorithm (Herman et al., 1976) for this study. The resulting 3D volume is interpolated within the acquisition angular range and extrapolated in the missing-wedge, resulting in ribbon-shaped reconstructions of dislocations. To extract linear contrast of dislocations, dislocation lines are redrawn directly into the reconstructed volume using the UCSF Chimera free software (Pettersen et al., 2004).

3. Results

3.1. *Presence of serpentine*

The microstructure of the studied peridotitic mylonite at the petrographic thin section scale was already recalled in section 2.1. Here, we focus on results not previously reported. The spinel-bearing harzburgite is very fresh for a specimen from a peridotite massif exhumed tectonically, and presents limited serpentinization (<1%) even if cracks along grain boundaries or cross-cutting grains are often found filled up with serpentine as illustrated by Fig. 2. However, the serpentinization is not ubiquitous at the micron scale and many grain boundaries remain closed and free of serpentine (Fig. 1f and e). Images at higher resolution using TEM again show that grain boundaries are mostly closed (Fig. 3a-b), some are open (Fig. 3c), not all being filled up with serpentine, but cracks can be found filled up with serpentine, cross-cutting deformed or underformed grains as illustrated by Fig. 3d and e. The occurrence of

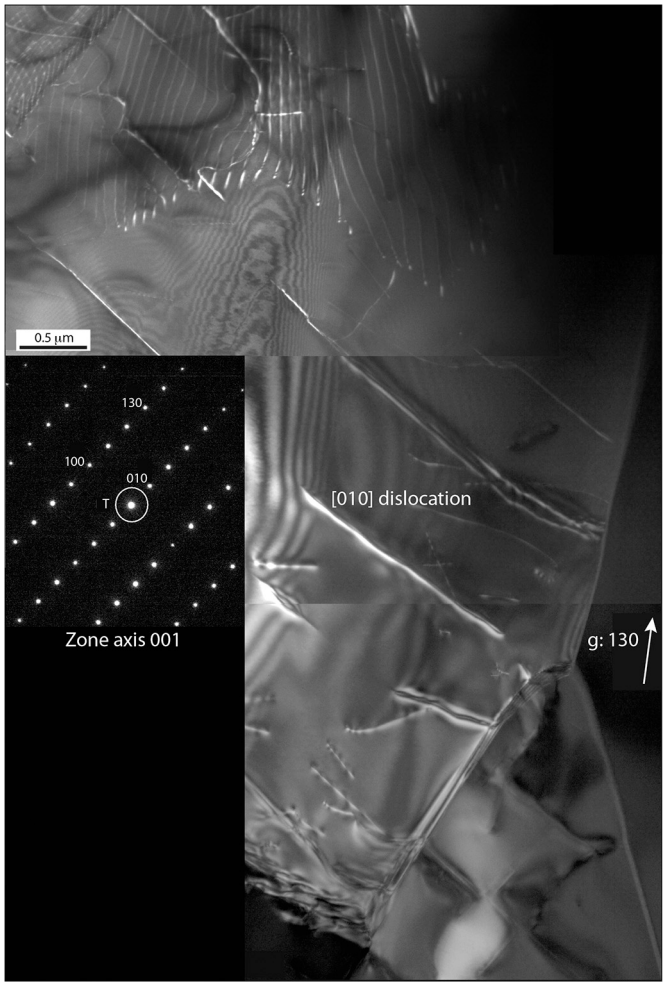

Fig. 6. Bright field TEM image of a complex junction between olivine grains. At the top left a flatten subgrain is almost adjacent to a triple junction at the bottom right. In weak-beam dark field, diffraction vector permits to identify [100] and [010] dislocation, with the latter having an important brightness when compared to the co-existing [100] dislocations.

serpentine was further established by selected area electron diffraction (SAED) into a serpentine-filled grain boundary (Fig. 3e) with diffraction patterns showing the 7.3 Å distance characteristic of crystal structures of serpentines (Yada, 1967; Dódony et al., 2002).

3.2. Type of dislocations and glide planes

Both small, newly formed, grains and olivine porphyroclasts were investigated. Representative WBDF TEM images of the dislocation microstructures are given in Figs. 4, 5 and 6. Both [100] and [001] dislocations are present in newly formed olivine grains (1–5 µm) and in porphyroclasts, but the newly formed olivine grains can either be free of dislocations (Fig. 4a) or containing [100] and [001] dislocations as illustrated by Fig. 4b-d with a dislocation density in the range of 10^{10}–10^{12} m^{-2}. Subgrain boundaries are easily found in porphyroclasts and are built from either [001] or [100] dislocations (Fig. 5). Dislocation densities in porphyroclasts are notably higher (3×10^{13} m^{-2} cf. Fig. 5a) than in newly formed grains. In olivine grains displaying evidence of both [100] and [001] slip activity, there is little evidence of interaction between the dislocations from the different slip systems. On rare occasion, [100] dislocation loops are found as shown in Fig. 5b-c. Furthermore, even [010] dislocations are also found perpendicular to a grain boundary of a deformed grain and in the vicinity of a triple junction as illustrated by Fig. 6. Note the three thickness fringes terminating at the tip of the dislocation indicating a high $g.b = |3|$ product, and thus a Burgers vector only compatible with a [010] dislocation. These [010] dislocations are predominantly of edge character.

We selected a representative sample volume illustrated in Fig. 7, containing both [100] and [001] dislocations (using diffraction vector $13\bar{1}$, see section 2.4.2) to further determine dislocation microstructure in 3D. First, the area is imaged in WBDF (Fig. 7a), then the volume is reconstructed in 3D (see supplementary material for an animation of the volume in 3D). Figs. 7b-g are projections for various tilt angles. Enlargements of some selected areas permit to further identify the habit planes of some dislocations (Fig. 7d-g). As evidenced in Fig. 7b, the number of [100] dislocations (in red) far exceeds that of [001] dislocations (in blue). Furthermore, [100] dislocations appear to be aligned close to the [001] direction. The short segments of [100] as well as [001] dislocations (Fig. 7b and c), which glide in (010) (Fig. 7e and f), are attesting to the activation of the [100](010) and [001](010) slip systems. The sub-grain boundary in the (100) plane (Fig. 7c) shown in the top left of Fig. 7a is composed of [100] dislocations. Note that in that case, indexation of the plane of the sub-grain boundary (Fig. 7c) was only possible thanks to the tomography since a tilt of 80° is physically inaccessible in the TEM and can only be achieved using a 3D reconstruction. In this study, we have not undertaken an exhaustive characterization of all slip planes present in the 3D reconstructed volume and slip systems imaged by tomography, however we have identified some remarkable configurations. In Fig. 7d, a [100] dislocation is lying close to the (100) plane which corresponds to the pure climb orientation. In Fig. 7g, a [100] dislocation is in a plane close to (210), which is neither a glide nor a climb plane, but an orientation in between evidencing a mixed climb configuration. The contribution of dislocation climb is further developed in the discussion section.

3.3. Melt

On rare occasions, the grain boundaries contain an intergranular amorphous phase as illustrated in Fig. 8. The area is composed of two newly formed, defect-free olivine grains (on the left) and a large porphyroclast on the right (same grain as in Fig. 5a). Imaging in diffuse dark field mode (Krivanek et al., 1979) shows a contrast characteristic of an amorphous phase that we interpret as a solidified melt. Note that the grain boundary between the two newly formed olivine grains on the left hand-side (white arrow in Fig. 8b) is apparently not containing a noticeable melt film.

3.4. Inclusions/bubbles

Few bubbles are found, connected to dislocations as illustrated Fig. 9, or located along grain boundaries or within the olivine matrix, with the latter not apparently linked to linear or planar defects. Note that their distribution is not matching typical planar arrays found for supercritical CO_2-bearing inclusions in olivine, nor display coalescence features (Roedder, 1965). Furthermore, not every olivine grain contains such bubbles. The occurrence of similar bubbles (in both size and distribution) was previously reported by Mackwell et al. (1985).

4. Discussion

4.1. Dislocations

The dislocations commonly found in the studied peridotite are in perfect agreement with previous studies on mantle-derived and naturally deformed studies for lithospheric temperatures (~1000 °C) as well as with experimentally deformed olivines at similar transition homologous temperature (e.g., Phakey et al., 1972; Green, 1976; Demouchy et al., 2013, 2014). Both [100] and [001] dislocations co-exist in both

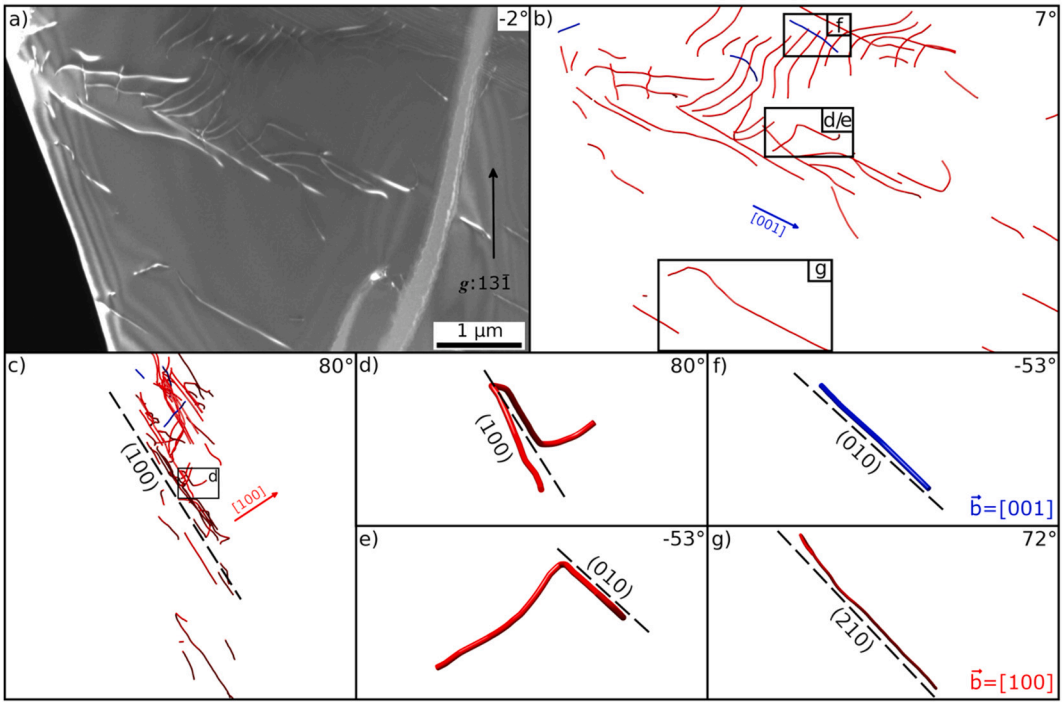

Fig. 7. Dislocation electron tomography characterization: (a) weak-beam dark field micrograph taken with the 13$\bar{1}$ diffraction vector at a projection angle of −2°, showing [100] and [001] dislocations; (b) reconstructed tomographic volume viewed at 7° showing [100] dislocations in red and [001] dislocations in blue as well as the [001] direction (black rectangles indicate dislocations which habit planes are edge-one in the corresponding subfigures); (c) reconstructed tomographic volume viewed with a projection angle of 80° showing the habit plane of the subgrain boundary edge-on, i.e. the (100) plane; (f) a [001] dislocation in (010) in the reconstructed volume oriented with a projection angle of −53°; (g) a [100] dislocation in a mixed climb plane (210) viewed with a projection angle of 72°; (d) and e) characterization of a 3D [100] dislocation where the upper part is in the (010) glide plane (seen at −53°) and the lower part is in the subgrain boundary (here visualized at 80°). See also supplementary material for an animation in 3D of the reconstructed tomographic volume. (For interpretation of the references to colour in this figure legend, the reader is referred to the web version of this article.)

porphyroclasts and newly formed olivines, without clear dominance of [100] dislocations relative to [001] dislocations, or the opposite (e.g., Demouchy et al., 2013; Thieme et al., 2018), but with little evidence of interaction between the dislocations from the different slip systems. This observation was also reported in previous studies (e.g., Durham et al., 1985). However, there is a clear difference between the dislocation density in porphyroclasts (3×10^{13} m^{-2}) and the one observed in average in the newly formed olivine (10^{10} m^{-2} to a maximum of 1×10^{12} m^{-2}). Interestingly, since newly formed olivine grains do not display well-structured subgrain boundaries, their dislocation density would be underestimated if quantified using EBSD using geometrically necessary dislocations as proxy for the total dislocation density (e.g., Cordier et al., 2014; Wallis et al., 2016; Demouchy et al., 2023). The origin of the plastic deformation undergone by these newly formed grains is likely to be late, but at temperatures ≥1000 °C, and linked to tectonic exhumation, post dynamic recrystallization at depths of lithospheric mantle.

Fortuitously, the studied sample permits to identify rare [010] dislocations in a dislocation-rich area, containing an almost in-plane subgrain boundary mostly composed of [100] dislocations (upper part of Fig. 6). We interpret thus the occurrence of these [010] dislocations as being constitutive of this subgrain boundary, hence being geometrically necessary dislocations rather than gliding dislocations. Previous report of [010] dislocations exist, but is essentially rare (Goetze and Kohlstedt, 1973; Boland and Liebermann, 1983; Fujino et al., 1993). Using high resolution TEM, Fujino et al. (1993) observed [010] dislocations in another mylonitic peridotite (Hidaka metamorphic belt, northern Japan) but equilibrated at 1100 °C (the authors show evidence of dissociation of these [010] dislocations). Furthermore, Fujino et al. (1993) report that only 1% of the total dislocations have $\boldsymbol{b}$ = [010]. In our study, such quantification of [010] dislocation density was not possible since they were found in only one grain.

Our observations have provided several evidence of the activation of dislocation climb under the natural deformation conditions experienced by this peridotite. The presence of sub-grain boundaries (see Figs. 5b, c, 6 and 7b, c) is a common argument for recovery, and we recall that it requires the activation of climb. Fig. 5b shows a subgrain boundary made of [100] dislocations and Fig. 5c shows two sub-grain boundaries parallel to (001) made of [001] dislocations. Additional evidence of climb are the dislocation loops (Fig. 5a, short white arrows), notably the [100] loop observed in Fig. 5b and c. Climb is also evidenced by the detailed analysis of a three-dimensional [100] dislocation shown in Figs. 7d and e. One segment of this dislocation is in a gliding configuration in (010) (Fig. 7e), but the rest of the dislocation lies in the subgrain boundary plane, parallel to (100), and hence is in a climb configuration (Fig. 7d). It remains impossible to determine, however, whether it is a [100] dislocation initially gliding in (010) and then being absorbed by climb into the subgrain boundary, or whether it is a dislocation from the subgrain boundary being emitted by glide in (010). More remarkable is the configuration in Fig. 7g, which shows a [100] dislocation moving in an intermediate plane between the plane of glide plane and the plane of pure climb. This type of configuration has

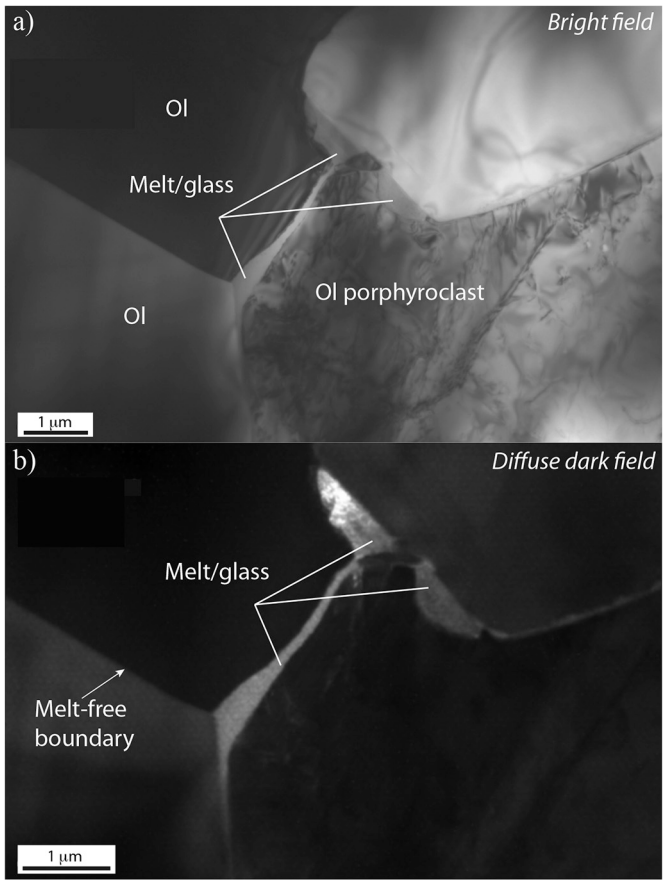

Fig. 8. (a) Bright field TEM image of two triple junctions between olivine (Ol) grains showing the presence of melt. Notes that the porphyroclastic grain, which is almost completely surrounded by melt, displays a high dislocation density relative to the two adjacent small (newly formed) olivines grains (on the left-hand side), which are almost dislocation-free; (b) Diffuse dark filed image showing the extent of melt distribution by density contrast.

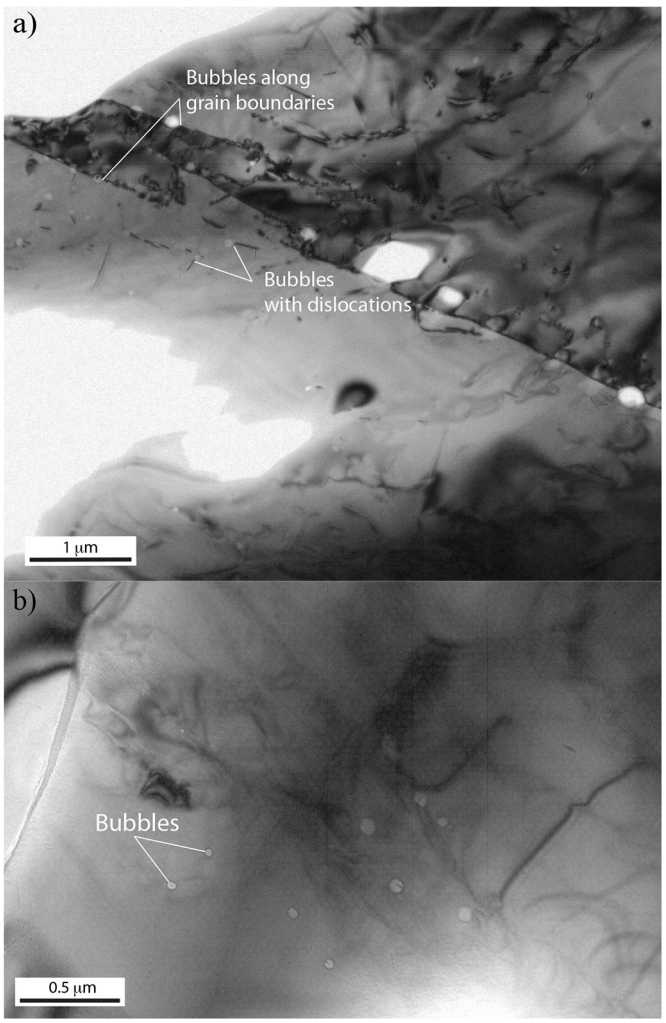

Fig. 9. Bright field TEM images of inclusion/bubble (a) located within olivine grains and at the tip of dislocations, or along olivine grain boundaries, or (b) within an olivine grain with no link to dislocation or planar defects.

recently been reported in TiAl alloys (Galy et al., 2023) and is now referred to as mixed climb. It shows that, under certain conditions relevant of the lithospheric mantle, the dislocation glide and climb velocities can be of the same order of magnitude. Such configurations have also been demonstrated in naturally deformed quartz (Mussi et al., 2021). This closer match between glide and climb velocities is probably a consequence of natural deformation conditions involving low stresses, which reduce glide velocity, and very low strain rates, which favor climb.

4.2. Occurrence of melt

Previous studies have already reported the low occurrence of melt in this type of mylonitic peridotite (Hidas et al., 2016; Ben Ismail et al., 2021). Here, we further confirm (Fig. 8) the occurrence of melt, but our TEM study cannot provide statistical data to assess the melt fraction or the melt-solid contact angle. Studies at broader scales, especially on the 3D distribution of melt using focused ion beam-SEM tomography, would then be required (e.g. Gardés et al., 2020).

5. Conclusion

We have reported an important diversity of dislocations in olivine naturally deformed at lithospheric conditions. Imaging by CTEM reveals that both newly formed grains and porphyroclasts display [100] and [001] dislocations activity, with little interactions, but also rare [010] dislocations, probably geometrically necessary. In olivine porphyroclasts, [100] loops are also observed. Electron tomography has permitted to identify [100](010) and [001](010) slip systems, and more importantly to assess the activation of climb. Our study further assesses the diversity of defects involved in plastic deformation at lithospheric conditions, including the level of heterogeneity of the microstructure, and thus heterogenous local strain where porphyroclasts with high dislocation density still co-exist with newly formed olivines. We recall that creep by dislocation glide and climb could be significantly different at asthenosphere conditions, where high temperatures will enhance ionic diffusion, and thus further enhance recovery mechanisms, notably climb and mixed climb.

Supplementary data to this article can be found online at https://doi.org/10.1016/j.pepi.2023.107125.

CRediT authorship contribution statement

Sylvie Demouchy: Conceptualization, Data curation, Formal analysis, Funding acquisition, Investigation, Methodology, Project administration, Writing – original draft, Writing – review & editing. **Alexandre Mussi:** Data curation, Formal analysis, Investigation, Methodology, Supervision, Validation, Visualization, Writing – review & editing. **Timmo Weidner:** Data curation, Formal analysis,

Investigation, Methodology, Validation, Visualization, Writing – review & editing. **Emmanuel Gardés:** Data curation, Formal analysis, Investigation, Writing – review & editing. **Patrick Cordier:** Conceptualization, Data curation, Formal analysis, Funding acquisition, Investigation, Methodology, Project administration, Supervision, Validation, Writing – original draft, Writing – review & editing.

Declaration of Competing Interest

The authors declare that they have no known competing financial interests or personal relationships that could have appeared to influence the work reported in this paper.

Data availability

Data will be made available on request.

Acknowledgments

We acknowledge funding from CNRS-INSU though their program TELLUS-Syster (project DOMINO 2021-2022) to SD; the European Research Council (ERC) under the European Union's Horizon 2020 research and innovation program under grant agreement No 787198 – TimeMan to PC. SD thank C. Nevado and D. Delmas for providing high-quality thin sections for TEM and SEM. S. Erdmann is thanked for her contribution for SEM images. The Helios SEM-STEM-FIB at CarMA facility at Université Clermont Auvergne is supported by the Conseil Régional Auvergne-Rhône-Alpes (France), and the TEM national facilities in Lille University is supported by the Conseil Régional du Hauts-de-France (France). Both microscopes are supported by the Institut National de Sciences de l'Univers (INSU) from Centre National de la Recherche Scientifique (CNRS, France).

References

Bai, Q., Kohlstedt, D.L., 1992. High-temperature creep of olivine single crystals, 2. Dislocation structures. Tectonophysics 206, 1–29. https://doi.org/10.1016/0040-1951(92)90365-D.

Bai, Q., Mackwell, S.J., Kohlstedt, D.L., 1991. High-temperature creep of olivine single crystals. 1. Mechanical results for buffered samples. J. Geophys. Res. 96, 2441–2463. https://doi.org/10.1029/90JB01723.

Barnard, J.S., Sharp, J., Tong, J.R., Midgley, P.A., 2006. High-resolution three-dimensional imaging of dislocations. Science 313, 319. https://doi.org/10.1126/science.1125783.

Ben Ismail, W., Mainprice, D., 1998. An olivine fabric database: an overview of upper mantle fabrics and seismic anisotropy. Tectonophysics 296, 145–157. https://doi.org/10.1016/S0040-1951(98)00141-3.

Ben Ismail, W., Tommasi, A., Lopez-Sanchez, M.A., Rutter, E.H., Barou, F., Demouchy, S., 2021. Deformation of upper mantle rocks with contrasting initial fabrics in axial extension. Tectonophysics 815, 228997. https://doi.org/10.1016/j.tecto.2021.228997.

Boioli, F., Carrez, P., Cordier, P., Devincre, B., Marquille, M., 2015a. Modeling the creep properties of olivine by 2.5-dimensional dislocation dynamics simulations. Phys. Rev. B 92, 014115. https://doi.org/10.1103/PhysRevB.92.014115.

Boioli, F., Tommasi, A., Cordier, P., Demouchy, S., Mussi, A., 2015b. Low steady-state stresses in the cold lithospheric mantle inferred from dislocation dynamics models of dislocation creep in olivine. Earth Planet. Sci. Lett. 432, 232–242. https://doi.org/10.1016/j.epsl.2015.10.012.

Boland, J.N., Liebermann, R.C., 1983. Mechanism of the olivine to spinel phase-transformation in Ni_2SiO_4. Geophys. Res. Lett. 10 (1), 87–90. https://doi.org/10.1029/GL010i001p00087.

Brey, G.P., Köhler, T., 1990. Geothermobarometery in four-phase lherzolith II. New thermobarometrers, and practical assessment of existing thermobarometers. J. Petrol. 31, 1353–1378. https://doi.org/10.1093/petrology/31.6.1353.

Carter, N.L., Ave'Lallemant, H.G., 1970. High-temperature flow of dunite and peridotite. Geol. Soc. Am. Bull. 81 (8), 2181–2202. https://doi.org/10.1130/0016-7606(1970)81[2181:HTFODA]2.0.CO;2.

Cordier, P., 2013. Characterization of dislocations and deformation processes by transmission electron microscopy. European Mineralogical Union Notes in Mineralogy 14, 67–107. https://doi.org/10.1180/EMU-notes.14.3.

Cordier, P., Demouchy, S., Beausir, B., Taupin, V., Barou, F., Fressengeas, C., 2014. Disclinations provide the missing mechanism for deforming olivine-rich rocks in the mantle. Nature 507, 51–56. https://doi.org/10.1038/nature13043.

Costa, F., Chakraborty, S., 2008. The effect of water in Si and O diffusion rates in olivine and implications for the transport properties and processes in the upper mantle. Phys. Earth Planet. Inter. 166, 11–29. https://doi.org/10.1016/j.pepi.2007.10.006.

Couvy, C., Frost, D., Heidelbach, F., Nyilas, K., Ungar, T., Mackwell, S., Cordier, P., 2004. Shear deformation experiments of forsterite at 11 GPa – 1400 °C in the multianvil apparatus. Eur. J. Mineral. 16 (6), 877–889. https://doi.org/10.1127/0935-1221/2004/0016-0877.

Demouchy, S., 2021. Defects in olivine. Eur. J. Mineral. 33, 249–282. https://doi.org/10.5194/ejm-33-249-2021.

Demouchy, S., Tommasi, A., Ballaran, T.B., Cordier, P., 2013. Low strength of Earth's uppermost mantle inferred from tri-axial deformation experiments on dry olivine crystals. Phys. Earth Planet. Inter. 220, 37–49. https://doi.org/10.1016/j.pepi.2013.04.008.

Demouchy, S., Mussi, A., Barou, F., Tommasi, A., Cordier, P., 2014. Viscoplasticity of polycrystalline olivine experimentally deformed at high pressure and 900 °C. Tectonophysics 623, 123–135. https://doi.org/10.1016/j.tecto.2014.03.022.

Demouchy, S., Thieme, M., Barou, F., Beausir, B., Taupin, V., Cordier, P., 2023. Dislocation and disclination densities in experimentally deformed polycrystalline olivine. Eur. J. Mineral. 35, 219–242. https://doi.org/10.5194/ejm-35-219-2023.

Dódony, I., Posfai, M., Buseck, P.R., 2002. Revised structure models for antigorite: an HRTEM study. Am. Mineral. 87 (10), 1443–1457. https://doi.org/10.2138/am-2002-1022.

Durham, W.B., Ricoult, D.L., Kohlstedt, D.L., 1985. Interaction of slip systems in olivine. In: Schock, R.N. (Ed.), Point Defects in Minerals. American Geophysical Union, Washington, pp. 185–193. https://doi.org/10.1029/GM031p0185.

Durinck, J., Devincre, B., Kubin, L., Cordier, P., 2007. Mesoscopic simulation of plastic slip in olivine. Am. Mineral. 92, 1346–1357. https://doi.org/10.2138/am.2007.2512.

Farla, R.J.M., Kokkonen, H., Fitz Gerald, J.D., Barnhoorn, A., Faul, U.H., Jackson, I., 2011. Dislocation recovery in fine-grained polycrystalline olivine. Phys. Chem. Miner. 38, 363–377. https://doi.org/10.1007/s00269-010-0410-3.

Fujino, K., Nakazaki, H., Momoi, H., Karato, S.-I., Kohlstedt, 1993. TEM observation of dissociated dislocation $\boldsymbol{b}$=[010] in naturally deformed olivine. Phys. Earth Planet. Inter. 78, 131–137. https://doi.org/10.1016/0031-9201(93)90089-R.

Gaboriaud, R.J., Darot, M., Gueguen, Y., Woirgard, J., 1981. Dislocations in olivine indented at low-temperatures. Phys. Chem. Miner. 7 (2), 100–104. https://doi.org/10.1007/BF00309460.

Galy, B., Musi, M., Hantcherli, M., Molénat, G., Couret, A., Spoerk-Erdely, P., Clemens, H., Monchoux, J.P., 2023. Glide and mixed climb dislocation velocity in γ-TiAl investigated by in-situ transmission electron microscopy. Scripta. Mat. 228, 115333 https://doi.org/10.1016/j.scriptamat.2023.115333.

Gardés, E., Laumonier, M., Massuyeau, M., Gaillard, F., 2020. Unravelling partial melt distribution in the oceanic low velocity zone. Earth Planet. Sci. Lett. 540 https://doi.org/10.1016/j.epsl.2020.116242.

Goetze, C., Kohlstedt, D.L., 1973. Laboratory study of dislocation climb and diffusion in olivine. J. Geophys. Res. 78, 5961–5971. https://doi.org/10.1029/JB078i026p05961.

Gouriet, K., Cordier, P., Garel, F., Thoraval, C., Demouchy, S., Tommasi, A., Carrez, P., 2019. Dislocation dynamics modelling of the power-law breakdown in olivine single crystals: toward a unified creep law for the upper mantle. Earth Planet. Sci. Lett. 506, 282–291. https://doi.org/10.1016/j.epsl.2018.10.049.

Green, H.W., 1976. Plasticity of olivine in peridotites. In: Wenk, H.R. (Ed.), Electron Microscopy in Mineralogy. Springer, Berlin, Heidelberg. https://doi.org/10.1007/978-3-642-66196-9_34.

Gueguen, Y., 1977. Dislocations in mantle peridotite nodules. Tectonophysics 89, 231–254. https://doi.org/10.1016/0040-1951(77)90098-1.

Gueguen, Y., 1979. Dislocation in naturally deformed terrestrial olivine: classification, interpretation, application. Bull. Mineral. 102, 178–183. https://doi.org/10.3406/bulmi.1979.7273.

Gueguen, Y., Darot, M., 1980. Microstructure and stresses in naturally deformed peridotites. Rock Mechanics suppl. 9, 159–172. https://doi.org/10.1007/978-3-7091-8588-9_17.

Gueguen, Y., Nicolas, A., 1980. Deformation in mantle rocks. Annu. Rev. Earth Planet. Sci. 8, 119–144. https://doi.org/10.1146/annurev.ea.08.050180.001003.

Herman, G.T., Lakshminarayanan, A.V., Naparstek, A., 1976. Convolution reconstruction techniques for divergent beams. Comput. Biol. Med. 6 (4), 259–271. https://doi.org/10.1016/00104825(76)90065-2.

Hidas, K., Tommasi, A., Garrido, C.J., Padrón-Navarta, J.A., Mainprice, D., Vauchez, A., Barou, F., Marchesi, C., 2016. Fluid-assisted strain localization in the shallow subcontinental lithospheric mantle. Lithos 262, 636–650. https://doi.org/10.1016/j.lithos.2016.07.038.

Holtzman, B.K., Kohlstedt, D.L., Zimmerman, M.E., Heidelbach, F., Hiraga, T., Hustoft, J., 2003. Melt segregation and strain partitioning: implications for the seismic anisotropy and mantle flow. Science 301, 1227–1230. https://doi.org/10.1126/science.1087132.

Idrissi, H., Bollinger, C., Boioli, F., Schryvers, D., Cordier, P., 2016. Low-temperature plasticity of olivine revisited with in situ TEM nanomechanical testing. Sci. Adv. 2, e1501671 https://doi.org/10.1126/sciadv.1501671.

Jung, H., Karato, S.I., 2001. Water-induced fabric transitions in olivine. Science 293, 1460–1463. https://doi.org/10.1126/science.1062235.

Karato, S.I., 1987. Scanning electron-microscope observation of dislocations in olivine. Phys. Chem. Miner. 14 (3), 245–248. https://doi.org/10.1007/BF00307989.

Kohlstedt, D.L., Goetze, C., Durham, W.B., Vandersande, J., 1976. New technique for decorating dislocation in olivine. Science 191 (4231), 1045–1046. https://doi.org/10.1126/science.191.4231.1045.

Kohlstedt, D.L., Bai, Q., Wang, Z.-C., Mei, S., 2000. Rheology of partially molten rocks. In: Bagdassarov, N., Laporte, D., Thompson, A. Bruce (Eds.), Physics and Chemistry of Partially Molten Rocks. Kluwer Academic Publisher, pp. 3–28. https://doi.org/10.1007/978-94-011-4016-4.

Krivanek, O.L., Shaw, T.M., Thomas, G., 1979. Imaging of thin intergranular phases by high-resolution electron-microscopy. J. Appl. Phys. 50 (6), 4223–4227. https://doi.org/10.1063/1.326453.

Mackwell, S.J., Kohlstedt, D.L., Paterson, M.S., 1985. The role of water in the deformation of olivine single crystals. J. Geophys. Res. 90 https://doi.org/10.1029/JB090iB13p11319, 11–319–11–333.

Mahendran, S., Carrez, P., Groh, S., Cordier, P., 2017. Dislocation modelling in Mg_2SiO_4 forsterite: an atomic-scale study based on the THB1 potential. Model. Simul. Mater. Sci. Eng. 25, 054002 https://doi.org/10.1088/1361-651X/aa6efa.

Mahendran, S., Carrez, P., Cordier, P., 2019. On the glide of [100] dislocation and the origin of "pencil glide" in Mg_2SiO_4 olivine. Philos. Mag. 99 (22), 2751–2769. https://doi.org/10.1080/14786435.2019.1638530.

McLaren, A.C., 1991. Transmission electron Microscopy of Minerals and Rocks - Cambridge Topics in Mineral Physics and Chemistry, Cambridge Topics in Mineral Physics and Chemistry, vol. 2. Cambridge University Press, p. 399. https://doi.org/10.1017/CBO9780511529382.

Miyajima, N., Li, Y., Abeykoon, S., Heidelbach, F., 2018. Electron channeling contrast imaging of individual dislocations in geological materials using a field-emission scanning electron microscope equipped with an EBSD system. Eur. J. Mineral. 30, 5–15. https://doi.org/10.1127/ejm/2017/0029-2683.

Mussi, A., Cordier, P., Demouchy, S., Vanmansart, C., 2014. Characterization of the glide planes of the [001] screw dislocations in olivine using electron tomography. Phys. Chem. Miner. 41, 537–545. https://doi.org/10.1007/s00269-014-0665-1.

Mussi, A., Cordier, P., Demouchy, S., 2015. Characterization of dislocation interactions in olivine using electron tomography. Philos. Mag. 95, 335–345. https://doi.org/10.1080/14786435.2014.1000996.

Mussi, A., Cordier, P., Demouchy, S., Hue, B., 2017. Hardening mechanisms in olivine single crystal deformed at 1090 °C: an electron tomography study. Philos. Mag. 97, 3172–3185. https://doi.org/10.1080/14786435.2017.1367858.

Mussi, A., Gallet, J., Castelnau, O., Cordier, P., 2021. Application of electron tomography of dislocations in beam-sensitive quartz to the determination of strain components. Tectonophysics. 803, 228754 https://doi.org/10.1016/j.tecto.2021.228754.

Nakamura, A., Schmalzried, H., 1983. On the nonstoichiometry and point defects of olivine. Phys. Chem. Miner. 10, 27–37. https://doi.org/10.1007/BF01204323.

Nicolas, A., Boudier, F., 1995. Mapping oceanic ridge segments Oman ophiolite. J. Geophys. Res. 100 (B4), 6176–6197. https://doi.org/10.1029/94JB01188.

Pettersen, E.F., Goddard, T.D., Huang, C.C., Couch, G.S., Greenblatt, D.M., Meng, E.C., Ferrin, T.E., 2004. UCSF chimera - a visualization system for exploratory research and analysis. J. Comput. Chem. 25 (13), 1605–1612. https://doi.org/10.1002/jcc.20084.

Phakey, P., Dollinger, G., Christie, J., 1972. Transmission electron microscopy of experimentally deformed olivine crystals. In: Heard, H.C., Borg, I.Y., Carter, N.L. (Eds.), Flow and Fracture of Rocks. American Geophysical Union. https://doi.org/10.1029/GM016p0117.

Philibert, J., 1991. Atom Movements - Diffusion and Mass Transport in Solids, Les Éditions de Physique, Les Ulis. ISBN: 2759801721.

Poirier, J.P., 1985. Creep of Crystals, High Temperature Deformation Processes in Metals, Ceramics and Minerals., Cambridge Earth Science Series. Cambridge University Press, Cambridge. https://doi.org/10.1017/CBO9780511564451.

Post, J.L., Borer, L., 2000. High-resolution infrared spectra, physical properties, and micromorphology of serpentines. Appl. Clay Sci. 16, 73–85. https://doi.org/10.1016/S0169-1317(99)00047-2.

Raleigh, C.B., 1968. Mechanism of plastic deformation of olivine. J. Geophys. Res. 73, 5391–5406. https://doi.org/10.1029/JB073i016p05391.

Rebled, J.M., Yedra, L., Estrade, S., Portillo, J., Peiro, F., 2011. A new approach for 3D reconstruction from bright field TEM imaging: beam precession assisted electron tomography. Ultramicroscopy 111, 1504–1511. https://doi.org/10.1016/j.ultramic.2011.06.002.

Roedder, E., 1965. Liquid CO_2 inclusions in olivine-bearing nodules and phenocrysts from basalts. Am. Mineral. 50, 1746–1782.

Schindelin, J., Arganda-Carreras, I., Frise, E., Kaynig, V., Longair, M., Pietzsch, T., Preibisch, S., Rueden, C., Saafeld, S., Schmid, B., Tinevez, J.Y., White, D.J., Hartenstein, V., Eliceri, K., Tomancak, P., Cardona, A., 2012. Fiji: an open-source platform for biological-image analysis. Nat. Methods 9, 676–682. https://doi.org/10.1038/nmeth.2019.

Thieme, M., Demouchy, S., Mainprice, D., Barou, F., Cordier, P., 2018. Stress evolution and associated microstructure during transient creep of olivine at 1000–1200 °C. Phys. Earth Planet. Inter. 278, 34–46. https://doi.org/10.1016/j.pepi.2018.03.002.

Wallis, D., Hansen, L.N., Ben Britton, T., Wilkinson, A.J., 2016. Geometrically necessary dislocation densities in olivine obtained using high-angular resolution electron backscatter diffraction. Ultramicroscopy. 168, 34–45. https://doi.org/10.1016/j.ultramic.2016.06.002.

Wenk, H.-R., 1976. Electron Microscopy in Mineralogy. Springer, p. 237. https://doi.org/10.1007/978-3-642-66196-9. ISBN: 978-3-642-66196-9.

Yada, K., 1967. Study of chrysotile by a high-resolution electron microscope. Acta Crystallogr. 23, 704–707. https://doi.org/10.1107/S0365110X67003524.